

RESEARCH ARTICLE

10.1002/2014JC009965

Key Points:

- A mooring located above the Mid-Atlantic Ridge influence by internal waves
- Internal waves may increase biological production
- Internal wave variability is taken into account in a one-dimensional model

Correspondence to:

G. Parard,
gaelle.parard@geo.uu.se

Citation:

Parard, G., J. Boutin, Y. Cuypers, P. Bouruet-Aubertot, and G. Caniaux (2014), On the physical and biogeochemical processes driving the high frequency variability of CO₂ fugacity at 6°S, 10°W: Potential role of the internal waves, *J. Geophys. Res. Oceans*, 119, 8357–8374, doi:10.1002/2014JC009965.

Received 12 MAR 2014

Accepted 31 OCT 2014

Accepted article online 6 NOV 2014

Published online 4 DEC 2014

On the physical and biogeochemical processes driving the high frequency variability of CO₂ fugacity at 6°S, 10°W: Potential role of the internal waves

Gaëlle Parard^{1,2}, J. Boutin¹, Y. Cuypers¹, P. Bouruet-Aubertot¹, and G. Caniaux³

¹LOCEAN, UMR7159, UPMC, CNRS, IRD, MNHN Paris, France, ²Department of Earth Sciences, University of Uppsala, Uppsala, Sweden, ³CNRM/GAME, Météo-France/CNRS, Toulouse, France

Abstract The availability of nutrients in the mixed layer is the main limitation to organic carbon biological production in the tropical regions. In this paper, we investigate the potential role of internal waves at promoting the development of biological activity on a PIRATA mooring at 6°S, 10°W. This mooring is located above the Mid-Atlantic Ridge where we observe strong internal waves. Using a one-dimensional physical and biogeochemical coupled model, we simulate dissolved inorganic carbon (DIC). Providing the influence of vertical advection and turbulent diapycnal diffusivity are (it is vertical advection + turbulent diapycnal mixing) accounted for, we find that this model provides a good fit with observed in situ CO₂ fugacity (fCO₂). Main effect of internal waves is to rapidly increase the DIC, thus the fCO₂ and the nutrients in the mixed layer. The latter induce progressive development of biological activity leading to gradual DIC decrease. Our study highlights the importance of correctly taking into account the effect of internal waves in tropical regions.

1. Introduction

The ocean plays an important role in the global carbon cycle [Wanninkhof *et al.*, 2013]. This role is strongly related to the physical and biological processes in the surface ocean [e.g., Gruber *et al.*, 2002]. It is well known that the input of limiting nutrients to the euphotic zone is a critical factor controlling primary production and the concentration of dissolved inorganic carbon (DIC) in the mixed layer. Several mechanisms have been identified as responsible for this transport such as (i) upwelling within mesoscale geostrophic eddies and submesoscale filaments and (ii) microscale three-dimensional turbulence generated by breaking internal waves (see a review in Lévy *et al.* [2012]). Moreover, the observation of such phenomena is laborious and expensive, due to the high resolution microstructure sampling required to elucidate these features. New time series of hourly CO₂ fugacity, fCO₂, are now available in various oceanic regions due to the recent development of autonomous fCO₂ sensors. Compared to the more traditional ship measurements, they provide new information on the influence of high frequency (hourly to few days) processes on fCO₂, in particular, the ones linked to the biological productivity [Boutin and Merlivat, 2009; Leinweber *et al.*, 2009; Parard *et al.*, 2010; Lefèvre and Merlivat, 2012; Thomas *et al.*, 2012]. In particular, biological productivity is strongly dependent on physical processes that influence the availability of light and nutrients in the photosynthetic zone. The goal of this paper is to understand the physical and biogeochemical processes responsible for the variability of fCO₂ observed at 6°S–10°W on a Prediction and Research moored Array in the Tropical Atlantic (PIRATA) mooring [Lefèvre *et al.*, 2008; Parard *et al.*, 2010]. This mooring is located above the Mid-Atlantic Ridge (Figure 1), which is one of the major topographic features in the Atlantic Ocean and is thought to be an important site for the generation of internal waves at the tidal frequencies (i.e., internal tides) [St. Laurent and Garrett, 2002; Egbert and Ray, 2003; Nycander, 2005]. Ocean regions with internal waves (as detected by Synthetic Aperture Radar (SAR)) often feature increased near-surface chlorophyll concentrations within bang-like structures. This suggests that internal waves act to advect the deep chlorophyll maxima toward the surface in midlatitude regions [Da Silva *et al.*, 2002]. It has also been suggested that internal waves may enhance biological productivity because they intensify vertical mixing and vertical nutrient fluxes [Kahru, 1983; Sharples *et al.*, 2001; Park *et al.*, 2008; Schafstall *et al.*, 2010]. However, the effect of internal waves on primary

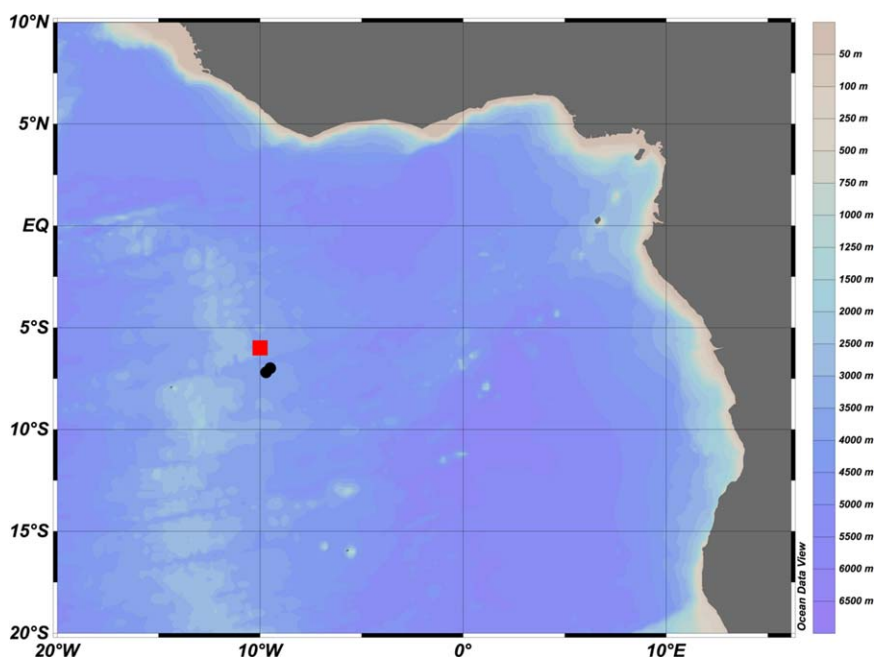


Figure 1. Location of the 6°S, 10°W PIRATA mooring (red square) where time series of $f\text{CO}_2$ and physical parameters were (the physical parameter and $f\text{CO}_2$ are collected) collected, superimposed on a bathymetric map (R. Schlitzer, Ocean Data View, <http://odv.awi.de>, 2012). We also used data gathered during EGEE cruises stations at that point. Argo locations are indicated in black dots (<http://www.coriolis.eu.org/Data-Products>).

production has rarely been quantified due to observational difficulties [Robinson and Da Silva, 2010]. Using high-resolution idealized numerical simulations, Liccardo *et al.* [2013] found that the vertically integrated productivity is increased at seasonal and shorter time scales when including short-term fluctuations in vertical diffusivity induced by internal wave breaking. Recently, a study [Muacho *et al.*, 2013] showed how the internal waves can affect primary production rates by enhancing the amount of biomass. The mechanism behind increased productivity appears to be increased levels of photosynthetically active radiation experienced by phytoplankton during upward vertical advection via internal wave dynamics. In this paper, we analyze for the first time the high frequency variability of $f\text{CO}_2$ and derived DIC concentration in a region that may be influenced by the occurrence of strong internal waves. This study is conducted at a PIRATA mooring where high frequency surface fluxes, physical, and carbon observations are available. These data allow us to carry out realistic simulations at temporal scales relevant to biogeochemical parameter variations. The influence of internal wave-induced vertical mixing and vertical advection is taken into account in a one-dimensional physical biogeochemical model which is forced by data from mooring measurements.

2. Observations

2.1. Data

The mooring at 6°S, 10°W (Figure 1) is a part of the PIRATA array [Bourlès *et al.*, 2008]. In this paper, we focus on a period in September 2006 for which the best vertical coverage of the upper water column is obtained. At the mooring, temperature was recorded at 10 min intervals at 1, 20, 40, 80, 100, 120, 140, 180, 300, and 500 m depths; whilst conductivity was recorded hourly at 1, 20, 40, and 120 m depths. In June 2006, a Carbon Interface Ocean Atmosphere (CARIOCA) sensor was added on the PIRATA mooring for measuring $f\text{CO}_2$ hourly at 1.5 m depth, with an accuracy of $\pm 3 \mu\text{atm}$ and a precision of $\pm 1 \mu\text{atm}$ [Lefèvre *et al.*, 2008; Parard *et al.*, 2010].

The total alkalinity (TA) is estimated from an empirical relationship between TA and SSS [Koffi *et al.*, 2010], with an accuracy of $\pm 7 \mu\text{mol kg}^{-1}$. DIC is derived from $f\text{CO}_2$ data and TA using the dissociation constants of Merbach *et al.* [1973] refitted by Dickson and Millero [1987] as in Parard *et al.* [2010] with an accuracy of $\pm 9 \mu\text{mol kg}^{-1}$ and a precision of $\pm 1 \mu\text{mol kg}^{-1}$.

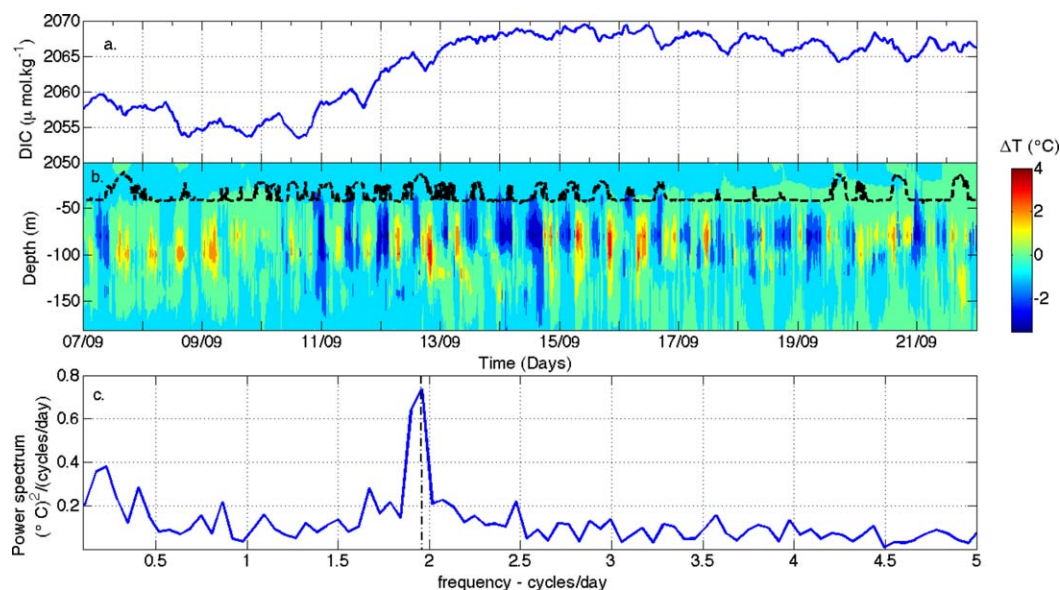


Figure 2. (a) DIC at 6°S , 10°W from 7 to 22 September 2006 and (b) Temperature anomalies at 6°S , 10°W . The black line indicates the mean mixed layer depth during the period. (c) Power spectrum of the temperature measured at 80 m. The vertical dashed line indicates the frequency of M2 tide.

Parard *et al.* [2010] have observed that during some periods fCO_2 diurnal and day-to-day variability is primarily influenced by sea surface temperature (SST) variations (hereafter called “physical period”) while during other periods, it is significantly influenced by biological activity (hereafter called “biological period”). This paper is dedicated to the study of the physical and biogeochemical processes at play during a period with strong biological activity.

2.2. Observed Processes

The period of investigation extends from 7 to 20 September 2006. It is characterized by a large variation of DIC (Figure 2). We divide this period into two different events. Before 11 September 2006, the variation of DIC is relatively small. From 11 to 15 September, DIC increases by $15 \mu\text{mol kg}^{-1}$ in about 5 days. Just after, from 16 to 20 September, we identify a “biological period,” during which the amplitude of the diurnal cycle of DIC is in phase with biological induced diurnal variability. During the “biological period,” the sea surface salinity (SSS) variations are <0.02 suggesting that horizontal advection at the surface plays a minor role allowing an estimate of net community production (NCP) as described in Boutin and Merlivat [2009]. During this period, the biological activity appears to be the main driver of the DIC and fCO_2 variability [Parard *et al.*, 2010]. The DIC (Figure 2) exhibits (i) clear diurnal cycles (peak-to-peak variation of about $3 \mu\text{mol kg}^{-1}$) in phase with sunset and sunrise, which are not in phase with the SST diurnal cycles and (ii) a day-to-day DIC decrease, a typical signature of net biological production [Parard *et al.*, 2010].

Observations of the temporal evolution of the temperature at varying depths highlights (Figure 2b) strong temperature anomalies at 40 m and deeper are observed with a conspicuous semidiurnal cycle (a peak is observed at 12.4 h on the spectrum of the temperature measured at 80 m (Figure 2c) between 7 and 17 September 2006 (Figure 2b)). The strong temperature anomalies near the base of the mixed layer from 10 to 15 September are associated with the DIC increase of $15 \mu\text{mol kg}^{-1}$ (Figure 2a) and a decrease of the daily temperature of 0.2°C .

The semidiurnal signal of the temperature anomaly is the signature of an internal tide with a dominant M2 (12.4 h) component, most likely generated at the Mid-Atlantic Ridge; the only strong generation spot of the M2 internal tide in the area [Nycander, 2005]. Indeed, internal waves may intensify the exchange of properties at the base of the mixed layer and could be a mechanism for the addition of dissolved nutrients (DN) to the mixed layer that could generate the “biological period.”

In the following, we study this period with a one-dimensional model, and focus on the impact of internal wave on the biogeochemistry parameters.

Table 1. Values of Diffusivity Coefficients in $m^2 s^{-1}$

Parameter	MLD	Under MLD	Reference
K_{TKE}	Mean value (0.07)	0	<i>Gaspar et al.</i> [1990]
K_{Cz}	0	4.09×10^{-4} (see equations (25), (26), and (27))	<i>Kantha and Clayson</i> [1994]
K_{iWSP}	0	1×10^{-5}	<i>Large et al.</i> [1994]
K_{iWV}	0	Variable with time and depth (mean value = 8.6151×10^{-5}) (see equations (4) and (5))	<i>Jardon et al.</i> [2011]

3. Physical-Biogeochemical Model

3.1. Model Description

For this study, a one-dimensional model is used. This model has been successfully applied for simulating diurnal variability of physical parameters observed at PIRATA moorings [e.g., *Dourado and Caniaux*, 2004; *Wade et al.*, 2010]. The

model simulates the temporal evolution of temperature and salinity with a time step of 10 min and a vertical resolution of 1 m over the upper 200 m [*Wade et al.*, 2010]. The physical model is derived from *Gaspar et al.* [1990] and improved by *Josse* [1992]. It can simulate the evolution of temperature, salinity, and horizontal velocity profiles in response to atmospheric forcing; in particular, it simulates well diurnal SST variations related to heat fluxes [*Wade et al.*, 2010].

The description of the model is detailed in Appendix A1. We couple this model with a biogeochemical model (see its description in Appendix A2) based on the model by *Taylor et al.* [1991], with particulate carbon (C, $mg\ C\ m^{-3}$) and one nutrient type (nitrate, DN, $\mu mol\ N\ L^{-1}$).

3.2. Parameterization of Turbulent Mixing Induced by Internal Waves and Vertical Advection

3.2.1. Vertical Diffusion Resulting From Internal Wave Breaking

In the reference model, two processes leading to turbulent mixing are taken into account below the mixed layer: shear instability of the current and internal wave breaking. Thus the vertical diffusion coefficient is the sum of two coefficients. The first one, K_{Cz} , mimics the effect of shear instability and is a function of the Richardson number. The second one, K_{iW} , mimics the effect of internal wave breaking and is set to a constant value equal to $10^{-5}\ m\ s^{-1}$ for temperature and salinity, and equal to $10^{-6}\ m\ s^{-1}$ for momentum [*Large et al.*, 1994] (Table 1). The latter parameterization is a crude estimate of turbulent diffusion and it largely underestimates turbulent diffusion when the energy level of the internal wave field is above that defined by *Garrett and Munk* [1975] model. Hence, we introduce a refined parameterization of this process, derived from the observations of temperature profiles available at the mooring, with a variable vertical diffusivity K_{iW} that depends on the energy of the internal wave field (Table 1). In this parameterization, the dissipation rate of turbulent kinetic energy, ϵ_{iW} , is inferred using the *Gregg-Henney* fine-scale parameterization [*Gregg*, 1989] based on shear variance and stratification. However, since we lack shear measurements here, following *Jardon et al.* [2011], we use a formulation in terms of available potential energy and stratification. Next K_{iW} is inferred from ϵ_{iW} following *Shih et al.* [2005] as detailed in the following.

The dissipation rate ϵ_{iW} is inferred as follows:

$$\epsilon_{iW} = 1.8 \times 10^{-6} \left(\frac{\langle PE \rangle^2}{PE_{GM}^2} \right) \left(\frac{N^2}{N_0^2} \right) \quad (1)$$

where N is the buoyancy frequency and $N_0 = 3\ cph$ is the canonical buoyancy frequency value, $\langle PE \rangle$ is a running average over two M2 periods of the available potential energy and PE_{GM} is the available potential energy of the *Garrett and Munk* internal wave field. The latter quantity depends on stratification only and is given by [*Gregg*, 1989]:

$$PE_{GM} = \frac{53}{2} N^2 \left(\frac{N}{N_0} \right)^{-1} \quad (2)$$

while the available potential energy, PE , is inferred from density fluctuations as follows [*Jardon et al.*, 2011]:

$$PE = \frac{g^2 \rho' 2}{2 \rho_0^2 N^2} \quad (3)$$

The density (ρ) is derived from the temperature and salinity time series measured at the mooring. As mentioned above, salinity measurements are not available at all depths in the thermocline. Here the values of

salinity at missing depths are computed from T data using the T/S relationship for the thermocline (correlation coefficient R equal to 0.99). The density anomaly ρ' is the difference between the density and the average density on the whole period at a given depth, the acceleration of gravity (g) is 9.81 m s^{-2} .

In a second step, according to *Shih et al.* [2005], we compute K_{iw} from the dissipation rate, ϵ_{iw} , according to two formulations depending on the intensity of turbulence:

1. For the intense turbulent regime when $\frac{\epsilon_{iw}}{vN^2} > 100$:

$$K_{iw} = 2v \left(\frac{\epsilon_{iw}}{vN^2} \right)^{\frac{1}{2}} \quad (4)$$

with the kinematic viscosity $v = 1.9 \times 10^{-6} \text{ m}^2 \text{ s}^{-1}$.

2. For regimes of intermediate turbulence intensity ($7 < \frac{\epsilon_{iw}}{vN^2} < 100$), the Osborn model is applied [*Osborn*, 1980]

$$K_{iw} = \gamma \left(\frac{\epsilon_{iw}}{N^2} \right) \quad (5)$$

where we assume $\gamma = 0.2$. The momentum mixing coefficient is taken as equal to K_{iw} divided by 10.

3.2.2. Estimate of Vertical Advection Induced by Internal Waves

The vertical velocity associated with internal waves can be calculated from the isotherm displacement estimated from the temperature anomalies computed for each depth

$$T' = T - \bar{T} \quad (6)$$

where \bar{T} is a running average of the local temperature over 10 days. Since most of the temperature variance is associated with internal waves at the semidiurnal M2 frequency and at the inertial frequency f (4.7 days), the temperature anomalies were filtered over a large frequency band from $0.8f$ to 1.4 times the M2 frequency. This procedure allows us to exclude (i) the effect of high frequency internal waves, which give a weak contribution to the temperature signal variance (see section 3.5) and are difficult to represent in the model and (ii) the long-term trend in the temperature stratification, which is not related to internal waves displacement. Isotherm displacements are then computed as:

$$\eta = \frac{T'_f}{\frac{\partial T}{\partial z}} \quad (7)$$

where T'_f are filtered temperature anomalies. The vertical velocity at depth $z + \eta$ is finally obtained as

$$\omega(z + \eta) = \frac{\partial \eta}{\partial t} \quad (8)$$

Vertical advection in the model is computed as $\omega \frac{\partial X}{\partial z}$, where $\frac{\partial X}{\partial z}$ is the vertical gradient of physical or biogeochemical variable X (temperature, salinity, chlorophyll, DIC, DN, etc.).

3.3. Atmospheric Forcing

The physical model is forced by the atmospheric surface fluxes. The radiative fluxes (short-wave and long-wave radiations) are measured at the PIRATA mooring. The turbulent heat fluxes are calculated every 10 min from atmospheric parameters (pressure, winds, humidity, and air temperature) and SST measured on the PIRATA buoy using the Exchange Coefficients from Unified Multicampaigns Estimates (ECUME) parameterization [*Weill et al.*, 2003]. This parameterization was derived from several campaigns completed under a large variety of atmospheric and oceanic conditions, and was found the most adequate to be used in our area [*Parard et al.*, 2010]. We used a constant albedo (0.05) and compute the upward infrared flux as $\epsilon \cdot \sigma \cdot \text{SST}^4$ with σ the Stefan-Boltzmann constant and ϵ the long-wave emissivity.

3.4. Model Initialization: Vertical Profiles

Between June 2005 and September 2007, six oceanographic Etude de la circulation océanique et de sa variabilité dans le golfe de Guinée (EGEE) cruises have been conducted as part of the Analyse Multidisciplinaire de la Mousson Africaine (AMMA) project in the eastern tropical Atlantic [*Redelsperger et al.*, 2006]. Vertical profiles of physical and biogeochemical parameters have been measured at the PIRATA mooring at 6°S , 10°W during EGEE cruises [*Bourlès et al.*, 2007]. Here we use vertical profiles of temperature, salinity (Figure 3), and fluorescence acquired with a Conductivity Temperature Depth (CTD) at 6°S , 10°W during EGEE 4 on 23 November 2006, 1 month after our study period. Vertical profiles of chlorophyll-a concentration (Figure 3)

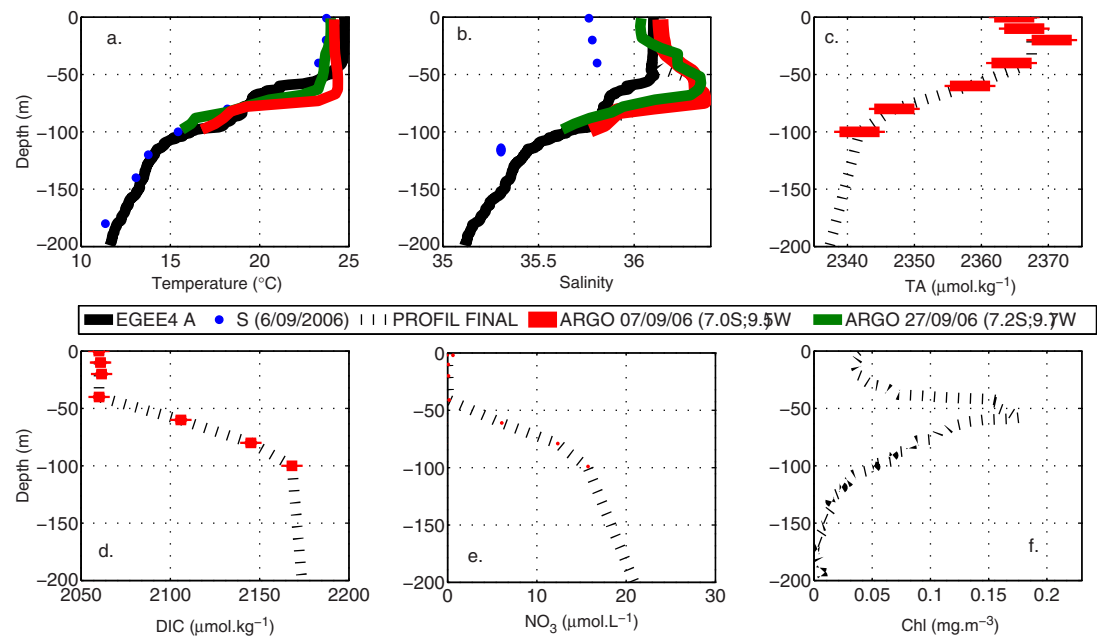


Figure 3. Vertical profiles measured or estimated of (a) temperature, (b) salinity, (c) TA, (d) DIC, (e) DN, and (f) Chl. (a and b) Solid line: EGEE 4 ascending CTD casts (ascending CTD casts have been used instead of the descending ones because DIC, TA, and DN were measured during the ascending cast and a large variability between ascending and descending profiles likely due to the passing of an internal wave were observed (Y. Gouriou, personal communication, 2011) (black) and ARGO profiles (red on 7 September 2006 at 7.0°S, 9.52°W and green on 27 September 2009 at 7.2°S, 9.7°W). Dots: PIRATA mooring measurements on 7 September 2006 (blue). (c–e) Measures from water samples during EGEE4 cruises and their associated errors (red). The profiles used for the simulation initialization are the measured EGEE4 profile for the temperature and the estimated profiles (dashed black line) for the other parameters.

have been estimated from the fluorescence profiles measured on the CTD, using a mean chlorophyll-fluorescence ratio derived from fluorescence and chlorophyll profiles measured during the EGEE 3 cruise. We find that surface chlorophyll ($\sim 0.2 \text{ mg m}^{-3}$) and chlorophyll profiles are consistent with, respectively, SeaWiFS chlorophyll value and typical profiles of this region [Herbland, 1983]. DIC, TA, and DN are measured from seawater samples taken during ascending CTD casts as described in Parard *et al.* [2010]. The mixed layer depth observed on these profiles is roughly consistent with the mooring measurements in September 2006.

On the other hand, salinity profiles recorded by ARGO floats close to the PIRATA moorings in September 2006 show a subsurface maximum (Figure 3b) which is not observed in EGEE initialization profiles. The subsurface salinity maximum has been observed during various cruises along 10°W [Kolodziejczyk *et al.*, 2009, Figure 2b] and is the signature of subtropical waters that probably originate from subduction of salty surface waters southwest of the mooring (N. Kolodziejczyk, personal communication, 2013). Hence, we modify the EGEE 4 salinity profile to include a subsurface salinity maximum (Figure 3b).

We maintain this subsurface maximum during the period of the simulations, by imposing a horizontal advection of salt in the subsurface maximum salinity layer [Wade *et al.*, 2010] of $V_{dy}^{\partial S} = 7 \times 10^{-7} \text{ s}^{-1}$. Temperature is simulated using the same scheme (with a horizontal advection of $V_{dy}^{\partial T} = 3 \times 10^{-6} \text{ } ^\circ\text{C s}^{-1}$). Likewise, DIC is simulated using a horizontal advection of $V_{dy}^{\partial DIC} = 7 \times 10^{-11} \text{ } \mu\text{mol kg}^{-1} \text{ s}^{-1}$ and DN with a horizontal advection of $V_{dy}^{\partial DN} = 2 \times 10^{-6} \text{ } \mu\text{mol L}^{-1} \text{ s}^{-1}$. The horizontal advection terms correspond to a current in the subsurface maximum salinity layer having a speed of about 0.3 m s^{-1} combined with T , S , DIC, and DN gradients of $0.0014 \text{ } ^\circ\text{C m}^{-1}$, 0.0028 m^{-1} , $2.8 \times 10^{-8} \text{ } \mu\text{mol kg}^{-1} \text{ m}^{-1}$, and $6.7 \times 10^{-6} \text{ } \mu\text{mol L}^{-1} \text{ m}^{-1}$, respectively. Given the small amount of data in the region, it is not possible to precisely validate these values, however their orders of magnitude are reasonably consistent with existing climatologies [Key *et al.*, 2004; Kolodziejczyk *et al.*, 2009; Garcia *et al.*, 2014].

3.5. Model Results

During the period under study, ω and K_{iv} derived from the measured density (cf. section 3.2) are on the order of typical measured values over the ocean [Planas *et al.*, 1999; Alford and Pinkel, 2000; Xie *et al.*, 2013].

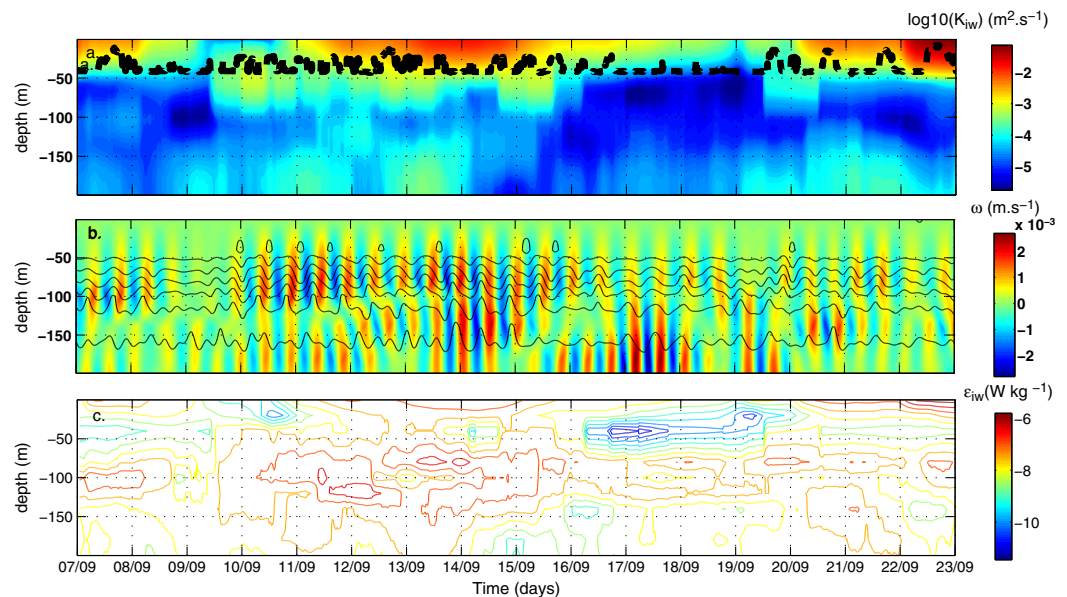


Figure 4. (a) Diapycnal turbulent vertical diffusivity coefficient (K_{iw}); the black dot line indicates the MLD estimated from the temperature profile at PIRATA mooring; (b) vertical velocity (ω) estimated from temperature and salinity measured at the mooring. The black lines correspond to the isopycnal displacements; and (c) dissipation rate (ϵ_{iw} derived from equation (1)).

They are particularly strong close to the base of the mixed layer (40 m) between the 10 and 16 September (Figure 4).

We run the model in two conditions described in section 3.2, one with the reference condition (REF) and the second with estimation of ω and K_{iw} from the data (IW) (Figure 4). To estimate the quality of the simulation, we used a correlation coefficient (R) and the root mean square difference (RMSD) computed over the entire period. The results are presented in Table 2.

The temperatures simulated at 40 and 80 m depth for the cases REF and IW are presented in Figure 5. The simulation IW reproduces better the strong variations of temperature at 40 and 80 m which are not reproduced in the REF simulation. As a consequence, R is higher and RMSD lower for the IW simulation (Table 2), especially at 80 m depth ($R = 0.61$ with IW simulation instead of $R = -0.02$ with the REF simulation).

At 1 m depth, the measured SSS increases between the 11 September and 15 September. This increase is not reproduced by the REF simulation but the simulation is improved in the IW version (Figure 6) and R is stronger in the IW simulation (0.84) (Table 2). For the SST from IW simulation, Table 2 shows a lower R but an improved RMSD. The slight decrease of the SST observed between 9 September and 12 September is not reproduced in either of the two simulations.

The DIC increases during the period of internal wave (Figure 2). The magnitude of this increase together with the diurnal cycles and day-to-day decrease during the “biological period” is quite well reproduced in the IW simulation compared to the REF simulation although the DIC increase is delayed by 1 day with respect to the observations (Figure 7). According to Table 2, the statistical parameters show an improvement of the DIC simulation in IW conditions with lower RMSD and higher R . In the REF simulation, the DN

Table 2. Difference of STD, Correlation Coefficient and RMS Difference Between Measured and Simulated Temperature for the Entire Period at 1, 40, and 80 m Depth, SSS, DIC, and fCO_2 at 1 m Depth

Parameter	Simulation	fCO_2	DIC	SSS	SST	$T(40\text{ m})$	$T(80\text{ m})$
R	REF	0.71	0.66	0.71	0.75	0.33	-0.02
	IW	0.73	0.82	0.84	0.31	0.53	0.61
RMSD	REF	5.86	6.76	0.03	-0.13	-0.34	-1.02
	IW	1.32	1.46	-0.003	0.01	-0.06	-1.5

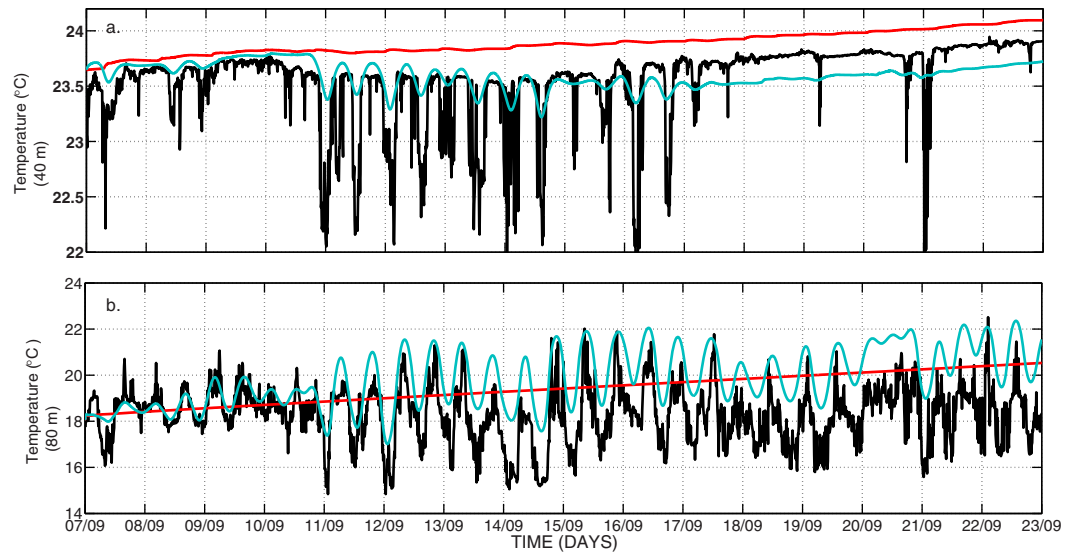


Figure 5. Temperature measured (black) and simulated at (a) 40 m and (b) 80 m depth with REF simulation (red) and with IW simulation (blue).

has a very low variation compared to the IW simulation. This difference can explain the improved simulation of DIC during the “biological period” in the IW case. A supply of DN to the mixed layer is needed to reproduce the biological cycle and day-to-day trend related to the net community production. This is consistent with the DN profiles sampled during EGEE that indicate low concentrations of nitrate in the mixed layer (between 0.07 and $0.2 \mu\text{mol L}^{-1}$). The IW simulation also improves the $f\text{CO}_2$ simulation (Figure 8 and Table 2). Contrary to simulated DIC, simulated $f\text{CO}_2$ increase is not delayed, because on day 1 in the $f\text{CO}_2$ computation the underestimate of DIC is compensated by the overestimate of SST.

In summary, these results show that the inclusion of the IW induced K_2 and ω in the simulations has two effects: (i) the increase of DIC in the mixed layer (around $15 \mu\text{mol kg}^{-1}$) and (ii) the increase of DN which allows the development of the “biological period” and leading to a decrease of DIC of around $2 \mu\text{mol kg}^{-1}$.

Our IW simulation (16–19 September) estimates NCP at $18 \text{ mmol m}^{-2} \text{ d}^{-1}$. We suggest that the difference between this value and the concurrent value of $26 \text{ mmol m}^{-2} \text{ d}^{-1}$ calculated by *Lefèvre and Merlivat [2012]*

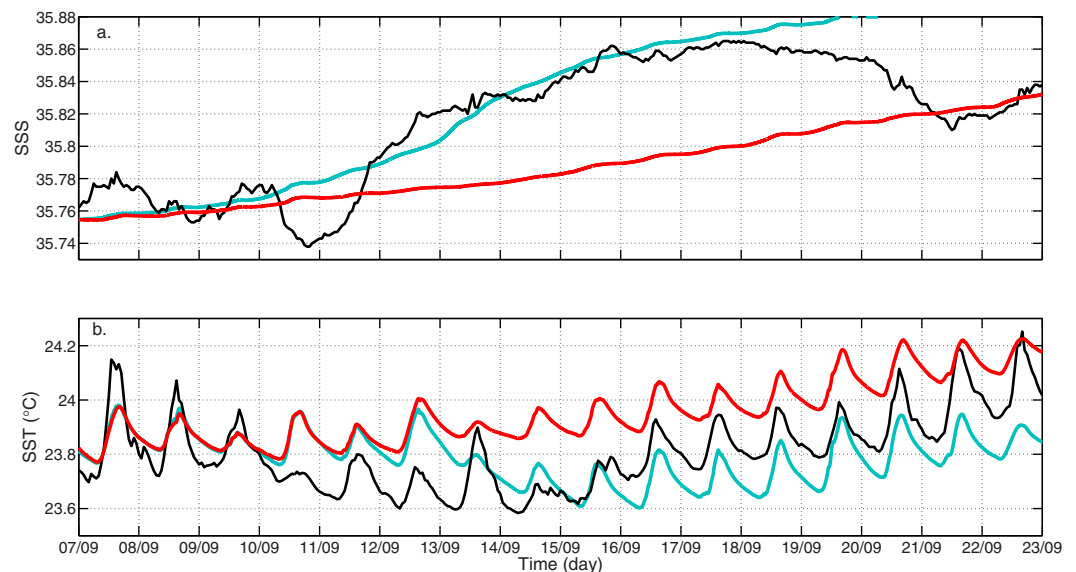


Figure 6. (a) SSS and (b) SST measured on PIRATA mooring (black) and simulated with REF simulation (red) and with IW simulation (blue).

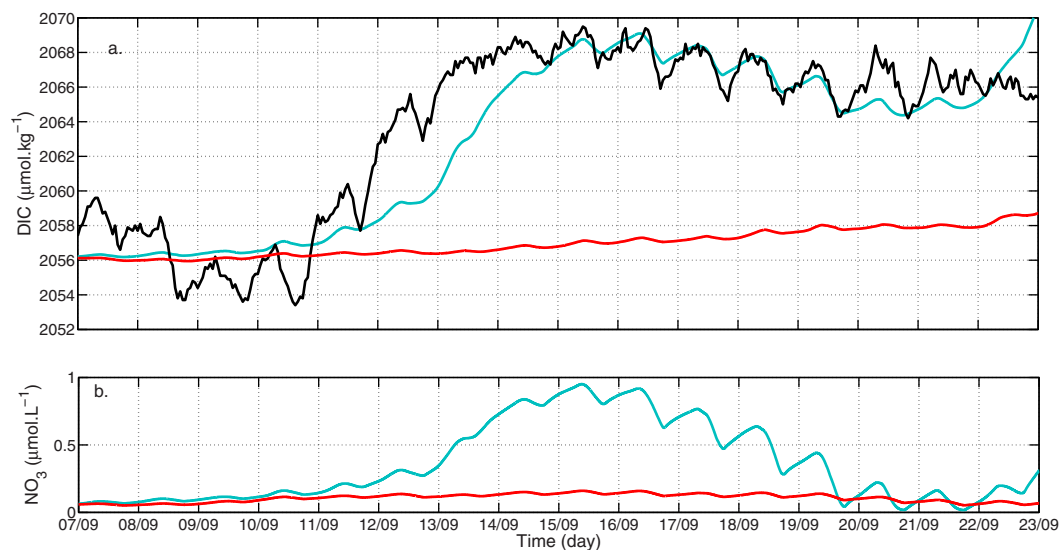


Figure 7. (a) DIC derived from measurements in black and DIC simulated with REF simulation (red) and with IW simulation (blue) and (b) NO_3^- simulated with REF simulation (red) and with IW simulation (blue).

(in agreement with *Parard et al.* [2010]) is due to differences in mixed layer depths (MLD) used. *Lefèvre and Merlivat* [2012] considered a not an but a MLD deeper (50 m) than the one estimated in this study from the model (37 m). The MLD from our model is in agreement with the one estimated with the interpolated temperature profile derived from PIRATA mooring measurements (36 m). The MLD is estimated with the temperature criteria of 0.2°C (difference between the surface and the bottom of the mixed layer) [*de Boyer Montégut et al.*, 2004]. The NCP estimated with the REF simulation is lower ($7 \text{ mmol m}^{-2} \text{ d}^{-1}$), indicating that the REF simulation does not adequately estimate the biological production.

Finally, we compute the air-sea CO_2 flux, for the IW and REF simulations using the method described in *Parard et al.* [2010]. The flux is underestimated in the case of the REF simulation ($0.3 \text{ mmol m}^{-2} \text{ d}^{-1}$ on the monthly flux). The difference observed between the two simulations varies from 0.1 to $1.7 \text{ mmol m}^{-2} \text{ d}^{-1}$. The average difference between IW and REF during the strong internal waves event is $1.5 \text{ mmol m}^{-2} \text{ d}^{-1}$, due to a change of 23% of the flux during 9 days.

4. Discussion and Conclusion

In order to perform realistic simulations of the biogeochemistry of the ocean mixed layer, it is crucial to realistically represent the exchanges of physical and biogeochemical properties between the ocean surface and subsurface. To the first order, in many cases, the hourly variability of $f\text{CO}_2$ can be explained by the diurnal variability of SST and the thermodynamical effect ($4.23\% \text{ }^\circ\text{C}^{-1}$) [*Takahashi et al.*, 1993]. Hence, simulating the hourly variability of $f\text{CO}_2$ requires the accurate modeling of sea surface temperature. At 6°S , 10°W where our study is focused, the physical model described in *Wade et al.* [2010] coupled with a biogeochemical model [*Lefèvre and Taylor*, 2002] allows the simulation of SST and $f\text{CO}_2$ with an accuracy of 0.04°C and $1.62 \text{ } \mu\text{atm}$, respectively. This accounts for explaining 69% of $f\text{CO}_2$ variability, during a 13 day period characterized by ocean surface warming and large diurnal cycles of SST [*Parard*, 2011]. Nevertheless, once the thermodynamical effect has been accounted for, some variability remains in surface DIC concentrations, in particular during other periods when biological production appears to be a dominant process. Indeed, *Parard et al.* [2010] and *Lefèvre and Merlivat* [2012] have suggested that some of these are linked to biological activity. However, the above mentioned models initialized with biogeochemical profiles measured during EGEE cruises do not allow to simulate the hourly and day-to-day variations of DIC, hence we have investigated the possible role of internal waves on biological activity. During some periods of high biological activity that appear to influence DIC [*Lefèvre and Merlivat*, 2012] occurred when internal waves have been detected from temperature data at various depths, leading to large K_{iw} values (Figure 9) close to the base of the mixed layer (between 40 and 60 m).

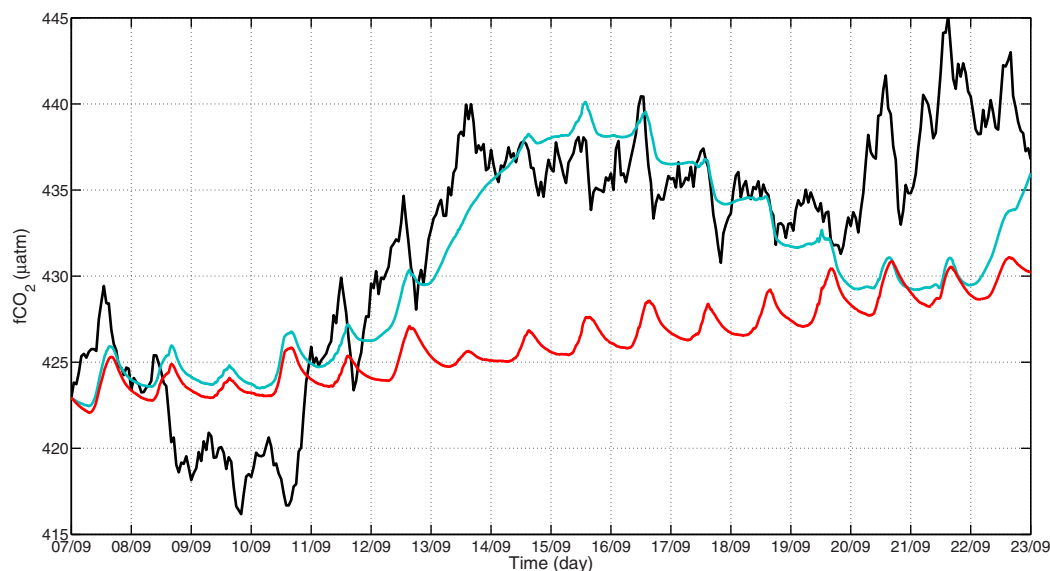


Figure 8. $f\text{CO}_2$ measurements (black) and $f\text{CO}_2$ simulated with REF simulation (red) and with IW simulation (blue).

Our study supports the hypothesis of a strong role of internal waves in supplying nutrients in the mixed layer enabling biological production. The impact of the vertical advection (not show here) is low compared to the one of K_{iw} . It represents 16% of the DIC variability, but is really important to simulate the temperature variability in the profile. We show that after occurrence of strong internal wave events, DIC variability simulated with the inclusion of internal waves processes very well agree with observations. We show that after occurrence of strong internal wave events, DIC variability simulated with the inclusion of internal waves processes very well agree with observations. The main effect of IW is to rapidly increase DIC, $f\text{CO}_2$, and DN in the mixed layer; then biological activity is enhanced and leads to a gradual decrease of DIC. The overall effect is an increase of mean DIC and $f\text{CO}_2$, and hence of the air-sea CO_2 flux.

Nevertheless, simulated DIC increase is delayed by about 24 h compared to the data. This may be linked to the response time of the model, i.e., a too slow exchange between the base of the mixed layer and the mixed layer. Actually, during the strong internal wave period (before the “biological period”), the model simulates an accumulation of cold water rich in DN and DIC at the base of the mixed layer. This supply of water with high DIC and DN decreases under the mixed layer when it increases in the mixed layer. There is a large uncertainty on the initial DIC gradient profile resulting from the coarse spatial resolution of the six measurements. This uncertainty is likely to affect the vertical distribution of the strong turbulent fluxes generated around 11 September and could induce the observed time lag in the DIC increase.

Nitrate availability is generally considered to be the limiting factor for oceanic biological production, in the studied region. We find that internal waves may increase biological production because they increase the exchange of nutrients between the mixed layer and the subsurface (contrary to midlatitude regions, their effect on light availability is negligible, as light is not a limiting factor for the biological production in this tropical region). During the study period, we compute the DN flux due to the impact of K_{iw} . The method used to compute the DN flux at the base of the mixed layer, is the same method used by Sharples *et al.* [2007]. In our case, we observe a mean DN flux of $0.6 \text{ mmol m}^{-2} \text{ d}^{-1}$ that varies between 0.3 and $1.5 \text{ mmol m}^{-2} \text{ d}^{-1}$. Bahamón *et al.* [2003] have reported upward nitrate flux of a similar magnitude ($0.53 \text{ mmol m}^{-2} \text{ d}^{-1}$) in the Northern Tropical Atlantic. They estimated K_{iw} using an assumption of a constant exponential decrease of the dissipation rate below the mixed layer combined with a constant mixing efficiency [Osborn, 1980]. Another study [Planas *et al.*, 1999] took place at 28°W along the transect 28°N and 35°S , which, like us, used the parameterization from Gregg [1989] and showed an increase of the DN flux due to the K_{iw} . They used vertical profiles of salinity and temperature derived from the CTD data and measurement of horizontal velocity. Between 9°S and 2°S , DN flux varies between 0.03 and $0.23 \text{ mmol m}^{-2} \text{ d}^{-1}$. Around the same latitude, the DN flux is lower than in our study. Nevertheless, closer to the Mid-Atlantic Ridge, they found a higher value (at 6.4°N : $1.5 \text{ mmol m}^{-2} \text{ d}^{-1}$).

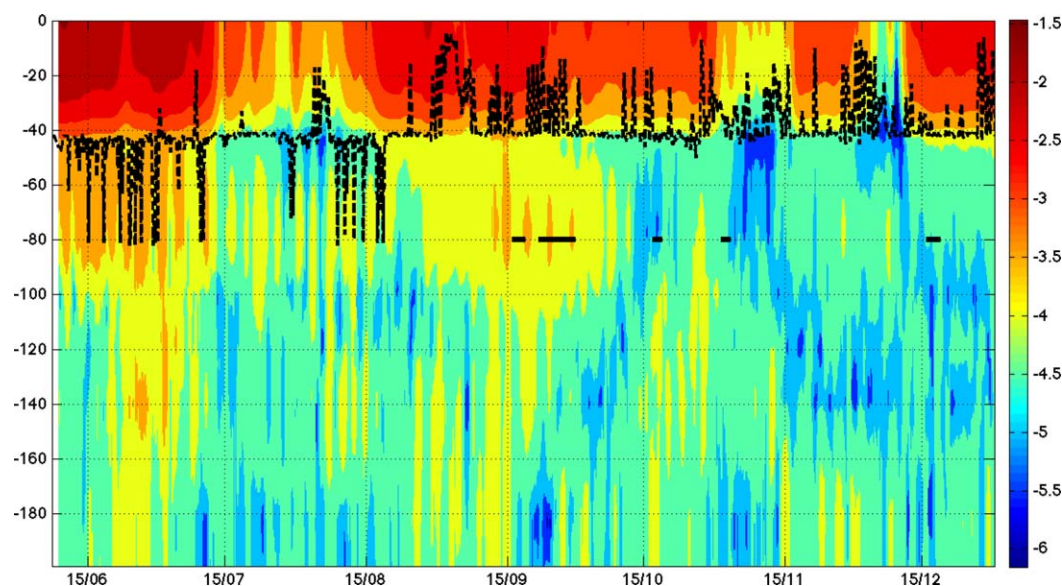


Figure 9. $\log(K_{iw})$ values ($\text{m}^2 \text{s}^{-1}$), from 6 June 2006 to 31 December 2006, derived from PIRATA temperature time series. Short black lines at 80 m water depth indicate biological periods as identified on DIC in Lefèvre and Merlivat [2012]. The black dashed line corresponds to the MLD estimated from the PIRATA temperature data.

Over a longer period (6 months), from 6 June to 31 December 2006, we have derived the DN flux at the base of the mixed layer to be $1.4 \text{ mmol m}^{-2} \text{ d}^{-1}$, using K_{iw} estimated from the PIRATA mooring at 6°S , 10°W and an averaged DN gradient from EGEE water samples. Introducing the variability of K_{iw} has a significant effect on the DN flux which is $0.1 \text{ mmol m}^{-2} \text{ d}^{-1}$ with the constant K_{iw} (10^{-5} in REF simulation). An estimation with a model [Oschlies, 2002], in the Equatorial Atlantic (8°S – 8°N), showed a lower mean nitrate flux ($0.76 \text{ mmol m}^{-2} \text{ d}^{-1}$) due to the vertical mixing. Compared to these studies, our results suggest that at the PIRATA site (where the internal tides are relatively strong), the internal waves induce vertical mixing that can significantly increase the nitrate flux.

Oschlies and Garçon [1998] stated that the eddy activity alone is not sufficient to maintain level of primary production and that an alternative mechanism should be considered. Our results suggest that internal waves mixing should also be considered.

Over 1 month (September), the effect of internal wave on air-sea CO_2 flux remains nevertheless relatively small ($0.3 \text{ mmol m}^{-2} \text{ d}^{-1}$, i.e., 5% of the monthly flux). Given the K_{iw} values derived from PIRATA mooring measurements (Figure 9), other periods in June, October, and December are also likely affected by internal waves. Using the same model as the one used in this study, the maximum effect on air-sea CO_2 flux would be simulated in June ($0.5 \text{ mmol m}^{-2} \text{ d}^{-1}$). However, assessing the impact of the cold tongue at the mooring during June is outside the scope of our model. Hence, quantifying the effect of internal wave on the air-sea CO_2 flux at a yearly scale would require the use of a three-dimensional model which is beyond the scope of this paper. It nevertheless suggests that one should pay more attention to the role of internal waves when dealing with biogeochemical simulations using physical-biogeochemical coupled models.

Appendix A: Physical-Biogeochemical Model

A1. Physical Model and Reference Parameterization

A physical model derived from Gaspar *et al.* [1990] and improved by Josse [1992] is used to simulate diurnal variability of physical parameters observed at PIRATA moorings [Dourado and Caniaux, 2004; Wade *et al.*, 2010]. The model simulates the temporal evolution of temperature, salinity, and horizontal velocity in response to atmospheric forcing, with a time step of 10 min and a vertical resolution of 1 m over the upper 200 m [Wade *et al.*, 2010]. Here we recall its main characteristics. The governing equations for the temperature (T), salinity (S), and horizontal velocity components (U , V) are

$$\frac{\partial T}{\partial t} = \frac{F_{sol}}{\rho_0 C_p} \frac{\partial l}{\partial z} - \frac{\partial}{\partial z} (\overline{T'\omega'}) - \omega \frac{\partial T}{\partial z} \tag{A1}$$

$$\frac{\partial S}{\partial t} = - \frac{\partial}{\partial z} (\overline{S'\omega'}) - \omega \frac{\partial S}{\partial z} \tag{A2}$$

$$\frac{\partial U}{\partial t} = fV - \frac{\partial}{\partial z} (\overline{U'\omega'}) \tag{A3}$$

$$\frac{\partial V}{\partial t} = -fU - \frac{\partial}{\partial z} (\overline{V'\omega'}) \tag{A4}$$

Here ω is the vertical component of the velocity, ρ_0 is a reference density (1024 kg m^{-3}), C_p is the heat capacity of sea water at constant pressure ($4178 \text{ J kg}^{-1} \text{ }^\circ\text{C}^{-1}$), F_{sol} is the net solar flux at the surface, and f is the Coriolis parameter. The operator \bar{X} denotes spatial and/or temporal averaging and $l(z)$ is fraction of F_{sol} which penetrates to the depth z [Paulson and Simpson, 1977]:

$$l(z) = R_a e^{-z/D1} + (1 - R_a) e^{-z/D2} \tag{A5}$$

Here D1 and D2 are the attenuation lengths and R_a denotes the red and infrared parts of downwelling solar irradiance, while the blue-green part is $1 - R_a$.

At the surface, the turbulent fluxes are specified as follows:

$$-\rho_0 C_p (\overline{T'\omega'})_0 = F_{nsol} = H + LE + F_{ir} \tag{A6}$$

$$-(\overline{S'\omega'})_0 = E - P \tag{A7}$$

$$-\rho_0 (\overline{U'\omega'})_0 = \tau_x \tag{A8}$$

$$-\rho_0 (\overline{V'\omega'})_0 = \tau_y \tag{A9}$$

where F_{nsol} represents the nonsolar heat flux, i.e., the sum of the sensible heat flux (H), the latent heat flux (LE), and the net infrared heat flux (F_{ir}). $E - P$ represents the net fresh water flux (evaporation minus precipitation), at the mooring. The term of precipitation is insignificant, and the term $E - P$ is mainly driven by evaporation, and $\tau_x(\tau_y)$ is the zonal (meridional) component of the wind stress.

Turbulence model: In equations (A1)–(A4), the turbulent fluxes are supposed to depend linearly on the local property gradients, through an eddy diffusivity K_X :

$$\overline{X'\omega'} = -K_X \frac{\partial X}{\partial z} \tag{A10}$$

Here $X \in \{U, V, T, S\}$. In the model, K_X is related to the local turbulent kinetic energy (TKE) ($\text{m}^2 \text{ s}^{-2}$), i.e., $e = (u'^2 + v'^2 + w'^2)/2$ via (i) a mixing length scale l_k determined by the minimum of the primary length scales which are the distances traveled upward (l_u) and downward (l_d) by a fluid particulate and (ii) a calibration constant $c_k = 0.1$ (the constant definitions are given in Table A1) [Gaspar et al., 1990]. The turbulent coefficient K_X corresponds to K_h , K_s , and K_m , respectively, for T , S and U , V :

$$K_m = c_k l_k \bar{e}^{1/2} \tag{A11}$$

$$K_s = K_h = \frac{K_m}{Pr} \tag{A12}$$

where Pr is the turbulent Prandtl number. To close the system of equations, the TKE equation is solved:

$$\frac{\partial \bar{e}}{\partial t} = - \frac{\partial}{\partial z} \left(\overline{e'\omega'} + \frac{\overline{p'\omega'}}{\rho_0} \right) - \left((\overline{u'\omega'}) \frac{\partial U}{\partial z} + (\overline{v'\omega'}) \frac{\partial V}{\partial z} \right) + \overline{b'\omega'} - \epsilon \tag{A13}$$

Here p is the pressure, ϵ is the dissipation of TKE, and $b = g(\rho - \rho_0)/\rho_0$ is the buoyancy with ρ the density. The water density is calculated from a linear version of the equation of state:

$$\rho = \rho_0 [1 - \alpha(T - T_0) + \beta(S - S_0)] \tag{A14}$$

where T_0 (S_0) is a reference temperature (salinity) and $\alpha(\beta)$ is a thermal expansion (haline contraction) coefficient. In equation (21), the sum of the vertical turbulent flux of TKE and of the term involving the correlation between pressure and vertical velocity fluctuations is parameterized by:

Table A1. Constants Definition in Physical Model (REF) Defined in Appendix A1

Name of the Constants	Prandtl Number P_r	C_c	C_k	Energy Minimum Under the ML	Proportionally Factor Between TKE Surface and Squared Friction
Value	1	1.43	0.1	$1 \times 10^{-6} \text{ m}^2 \text{ s}^{-2}$	$\text{TKE} = u^{*2}$

$$-\left(\overline{e'w'} + \frac{\overline{p'w'}}{\rho_0}\right) = K_e \frac{\partial \bar{e}}{\partial z} \tag{A15}$$

where $K_e = K_m$. The dissipation term ϵ is parameterized using the *Kolmogorov* [1942] theory, i.e., $\epsilon = c_\epsilon \bar{e}^{3/2} / l_\epsilon$ where $c_\epsilon = 1.43$ (Table A1) is another calibration constant and l_ϵ a the characteristic length of dissipation [Bougeault and Lacarrere, 1989].

In the reference parameterization, mixing can be produced below the mixed layer, under the effect of strong current shear by the Kelvin-Helmoltz instability mechanism [Large et al., 1994]. Current shear causes a reduction of the Richardson gradient number, increases the instability, and intensifies mixing [Kantha and Clayson, 1994], as described in Dourado and Caniaux [2004]. In addition, internal waves can generate turbulence in stratified layers as they break, leading in some cases to intensified mixing at the base of the mixed layer. Internal waves can generate turbulence in stratified layers or when propagating into other areas, they can intensify the mixing between the homogeneous mixed layer and the thermocline [Alford, 2003]. In this model, the mixing under the mixed layer is taken as a superposition of these two processes: the instability due to the vertical shear of the current (leading to an effective diffusivity K_{cz}), and the instability due to the internal waves (K_{iw}). The vertical mixing coefficient is a sum of these two terms. K_{cz} is a function of the Richardson number (Ri) and K_{iw} is assumed constant and equal to 10^{-5} m s^{-1} for temperature and salinity, and equal to 10^{-6} m s^{-1} for the momentum [Large et al., 1994].

In the model K_{cz} is define in function of Ri :

$$Ri = \frac{g \frac{\partial \rho}{\rho \partial z}}{\frac{\partial U^2}{\partial z}} \tag{A16}$$

If $Ri > 0.7$:

$$K_{cz} = 0 \tag{A17}$$

if $0 < Ri < 0.7$:

$$K_{cz} = 5 \times 10^{-3} \left[1 - \left(\frac{Ri}{0.7} \right)^2 \right]^3 \tag{A18}$$

if $Ri < 0$:

$$K_{cz} = 5 \times 10^{-3} \tag{A19}$$

A2. Biogeochemical Model

The biogeochemical model is based on Taylor et al.'s [1991] model, with a representation of the particulate carbon (C , mgC m^{-3}) and one type of nutrient (nitrate, DN , mmol N m^{-3}). The governing equations are

$$\frac{\partial C}{\partial t} = [-(m + R_r) + P^C] C + \frac{\partial}{\partial z} \left[K \frac{\partial C}{\partial z} \right] \tag{A20}$$

$$\frac{\partial DN}{\partial t} = \gamma [\epsilon_f (m + R_r) - P^C] C + \frac{\partial}{\partial z} \left[K \frac{\partial DN}{\partial z} \right] \tag{A21}$$

Here m and R_r are, respectively, the mortality and the phytoplankton respiration rate in d^{-1} , γ is the conversion factor from mgC in mmol N (based on a C:DN ratio of 5.6), and K is the turbulent diffusion coefficient (the same value is taken for physical and biogeochemical variables). The recycling efficiency, ϵ_f , is assumed to be a function of the local nutrient concentration:

$$\epsilon_f = 0.3 + \frac{(\epsilon_{fmax} - 0.3)K_N}{DN + K_N} \quad (A22)$$

ϵ_{fmax} is the maximum recycling efficiency when DN becomes depleted; in this case, ϵ_f ranges between 0.3 and ϵ_{fmax} . K_N is the half-saturation constant for nitrate uptake. P^C is the carbon-specific photosynthesis rate (in d^{-1}); it is function of irradiance (I):

$$P^C = P_m^C \exp \left[\frac{-E_a}{R} \left(\frac{1}{T} - \frac{1}{T_{ref}} \right) \right] \left[1 - \exp \left(-\frac{\alpha_{chl} I \theta}{P_m^C} \right) \right] \quad (A23)$$

$$P_m^C = P_{max}^C \frac{DN}{DN + K_N} \quad (A24)$$

Here P_m^C is the light saturation rate of photosynthesis normalized to carbon (in d^{-1}), P_{max}^C is the value of P_m^C at the reference temperature $T_{ref} = 25^\circ C$, α_{chl} is the initial slope of the photosynthesis-irradiance (P-I) curve normalized to Chl, θ is the Chl:C ratio, $E_a = 7000 J mol^{-1}$ the activation energy, $R = 8.3 J mol^{-1} K^{-1}$ is the universal gas constant, and T is the temperature.

We use a variable θ as suggested by Geider *et al.* [1997]; in this case, the model conditions vary and we add the following equation:

$$\theta = \theta_{initial} \left[\frac{1}{1 + \frac{(\theta_{initial} \alpha_{chl} I)}{(2P_m^C)}} \right] \quad (A25)$$

We chose $\theta_{initial} = 1/40 gChl gC^{-1}$ which is close to the values used by Lefèvre *et al.* [2003], Tyrell and Taylor [1995], and Voituriez and Herbland [1977] and close to the value observed in the Equatorial Pacific [Wang *et al.*, 2009]. With this parameterization, the Chl and C vary in a nonconstant ratio

$$\frac{\partial Chl}{\partial t} = [-(m + R_r)Chl + \rho_{chl} P^C C] + \frac{\partial}{\partial z} \left[K \frac{\partial Chl}{\partial z} \right] \quad (A26)$$

with ρ_{chl} the ratio of Chl synthesis to carbon fixation:

$$\rho_{chl} = \theta_{initial} \left[\frac{P^C}{(\theta \alpha_{chl} I)} \right] \quad (A27)$$

The evolution equation of DIC:

$$\frac{\partial DIC}{\partial t} = [\epsilon(m + R_r) - P^C] \Gamma_C C + \frac{\partial}{\partial z} \left[K \frac{\partial DIC}{\partial z} \right] \quad (A28)$$

$$\frac{\partial DIC_{surf}}{\partial t} = [\epsilon(m + R_r) - P^C] \Gamma_C C + \frac{\partial}{\partial z} \left[K \frac{\partial DIC}{\partial z} \right] + K_h (p_{air} - p_{water}) \frac{1}{\partial z} \quad (A29)$$

In the surface layer, the DIC evolution is expressed by equation (37) where K_h is the CO_2 exchange coefficient derived from the Sweeney *et al.* [2007] relationship, and $p_a(p_w)$ the atmospheric (surface seawater) partial pressure of CO_2 ; it is computed from the data as described in Parard *et al.* [2010]. Γ_C is the increase of carbon concentration when $1 mg Chl m^{-3}$ is produced and is taken equal to $1.23 \times 10^{-5} \mu mol kg^{-1} m^3 g^{-2}$. The equation describing the temporal evolution of TA is:

$$\frac{\partial TA}{\partial t} = \Gamma_A \gamma [P^C - \epsilon(m + R_r)] C + \frac{\partial}{\partial z} \left[K \frac{\partial TA}{\partial z} \right] \quad (A30)$$

Γ_A is the conversion factor to change from $mmol N m^{-3}$ in $\mu mol kg^{-1}$ and is taken equal to 1.1×10^{-6} . fCO_2 is calculated from DIC and TA and the dissociation constant of Merbach *et al.* [1973] refitted by Dickson and Millero [1987]. The biogeochemical model is initialized by vertical profiles of DIC, TA, DN, Chl based on measurements gathered during EGEE campaigns (see section 3.4); DIC and TA profiles used for the model initialization are shifted by a constant value to fit the value estimated at the beginning of the simulation.

A3. Adjustment of Biological Parameters at the PIRATA Mooring

After some sensitivity tests on the influence of initialization profiles and atmospheric fluxes (not shown here), we conduct sensitivity tests on the biological parameters. The sensitivity tests allow us to quantify the effect of each biological parameter and to evaluate its ability at reproducing the observed DIC. For these

Table A2. List of Values for Parameters Optimized for the Biological Parameterization^a

Parameter	Definition	Range	Reference	Optimized Value
α_{chl}	Initial slope of the photosynthesis-irradiance [Geider et al., 1998; Lefèvre and Taylor, 2002; Lefèvre et al., 2003; Taylor et al., 1991]	$0.5 \times 10^{-5} - 1.5 \times 10^{-5}$ gC (gChla $\mu\text{mol kg}^{-1}$) ⁻¹	7.5×10^{-5} gC (gChla $\mu\text{mol kg}^{-1}$) ⁻¹	1.5×10^{-5} gC (gChla $\mu\text{mol kg}^{-1}$) ⁻¹
m	Mortality	Variable along the depth between 0 and 1 d ⁻¹	$m = 0.4$ d ⁻¹ (0–60 m)-between 60 m and 120 m, m linearly decreases to $m = 0$ d ⁻¹ below 120 m	$m = 0.9$ d ⁻¹ (0–50 m) $m = -0.0067z + 0.73$ d ⁻¹ (50–110 m) $m = 0$ d ⁻¹ (below 110 m)
R_r	Respiration rate [Geider et al., 1998; Lefèvre and Taylor, 2002; Lefèvre et al., 2003; Taylor et al., 1991]	0 d ⁻¹ –1 d ⁻¹	0.1 d ⁻¹	0.27 d ⁻¹
P_{cmax}	Light saturation rate of photosynthesis normalized to carbon [Geider et al., 1998; Lefèvre et al., 2003]	0 d ⁻¹ –5.1 d ⁻¹	1.5 d ⁻¹	5.1 d ⁻¹
$\frac{1}{\theta}$	Carbon: chlorophyll ratio [Geider et al., 1997]	20–120 gC gChl ⁻¹	Constant $\frac{1}{\theta} = 40$ gC gChl ⁻¹	$\frac{1}{\theta_{initial}} = 40$ gC gChl ⁻¹ variable along time

^aFor the other parameters in the biogeochemical model, the values are presented in Lefèvre and Taylor [2002, Table A1].

tests, we focused on the biological event which takes place during our study period, between 16 and 20 September 2006. The adjusted parameters are listed in Table A2; we also recall the range of the parameters considered in previous publications [Geider et al., 1998; Lefèvre and Taylor, 2002; Lefèvre et al., 2003; Taylor et al., 1991] that have made use of Taylor’s biological model for simulations at the seasonal scale. The sensitivity tests are performed in two steps. First, all of the parameters are set to the values used in the Atlantic gyres by Lefèvre and Taylor [2002] (called in the following the reference value) except one parameter which we allow to vary within the range previously defined.

In these first-step simulations, we use a Taylor diagram [Taylor, 2001] in order to evaluate the quality of the simulations relative to the observations (Figure A1). The similarity between the observations and the model results is quantified with Taylor diagram in terms of their correlation between the test and reference fields, their centered root-mean-square difference (RMSD) and the amplitude of their variations (represented by their standard deviation (STD) of their difference). The RMSD between the simulations and observations patterns is proportional to the distance to the point on the x axis identified as “Buoy.” Hence, the best simulations are the ones that lie nearest the point marked “Buoy” on the x axis. The green contours indicate the RMSD values and it can be seen that the RMSD range between 0.6 and 1.5 $\mu\text{mol kg}^{-1}$. STD is lower for all tests than the observed STD (1.2 $\mu\text{mol kg}^{-1}$), which show that the amplitude of DIC variations is lower for the simulations compared to the observation (Figure A1).

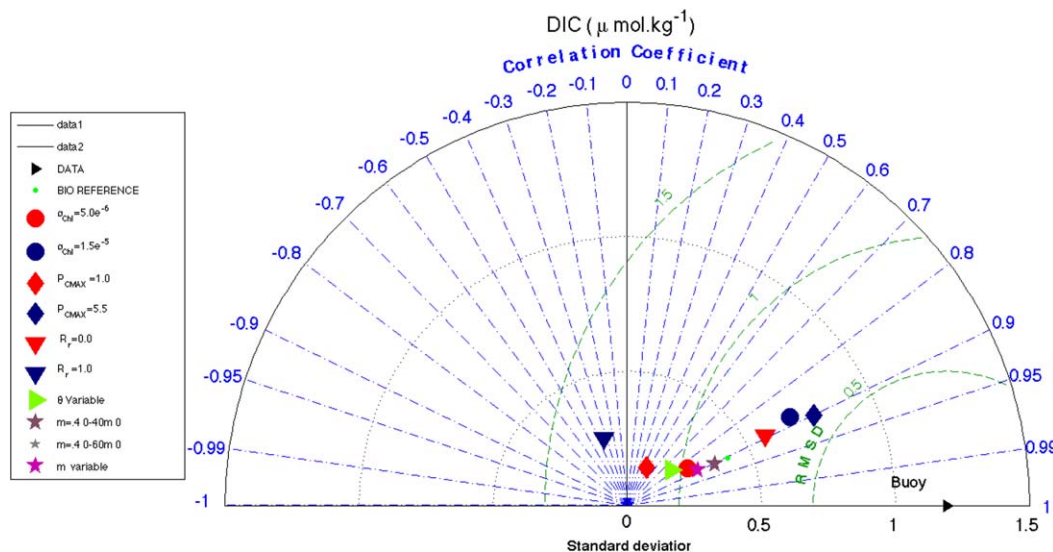


Figure A1. Taylor diagram for the biological period 16–20 September 2006 at 1 m depth. Differences between DIC simulations tests are represented by the symbols (see legend inside this figure) and data are represented by the black triangle and are called Buoy. The range of each parameters is close to the literature values presented in Table A2.

Three parameters have a strong impact on the simulation. P_{cmax} , α_{chl} , and R_r improve the DIC simulation for R_r low, P_{cmax} , or α_{chl} high. In these cases, the RMSD, the correlation coefficient, and STD are improved, i.e., RMSD is higher than $0.5 \mu\text{mol kg}^{-1}$, the correlation coefficient is high (0.9), and the STD is close to the STD of observation. In Figure A1, these three tests are the closest points from the “Buoy.” The amplitude of the DIC diurnal cycle at the mooring is better simulated when P_{cmax} and α_{chl} are maximized.

Once P_{cmax} and α_{chl} have been adjusted to improve the simulation of DIC in terms of standard deviation and correlation with observations, R_r and m have been increased in order to keep a realistic value for the concentration of phytoplankton. Furthermore, we use a variable θ [Geider *et al.*, 1998], which further improves the DIC simulation. The final adjusted values are indicated in Table A2.

The adjusted α_{chl} value of $1.5 \times 10^{-5} \text{ gC (gChla } \mu\text{mol kg}^{-1})^{-1}$ appears to be consistent with existing estimates of the photosynthetic characteristics of the major species of phytoplankton in the tropical Atlantic in particular species from the picoplankton *Prochlorococcus* or *Synechococcus* [Robinson *et al.*, 2002]. For these species, α_{chl} remains poorly contained; it is commonly in the range between 8.6×10^{-6} and $38.99 \times 10^{-6} \text{ gC (gChla } \mu\text{mol kg}^{-1})^{-1}$, or even larger for some species. This parameter varies strongly with the availability of light [Veldhuis *et al.*, 2005].

The value of $\frac{1}{\theta}$ in our simulations ranges between 40 and $150 \text{ gC gChla}^{-1}$. Very few studies of θ exist for the tropical Atlantic. In the northern tropical Atlantic, Veldhuis *et al.* [2005] found $\frac{1}{\theta}$ ranging between 21 gC gChla^{-1} around 150 m depth and $450 \text{ gC gChla}^{-1}$ near the ocean surface for *prochlorococcus*. In the equatorial Pacific, Wang *et al.* [2009] found $\frac{1}{\theta}$ values ranging between 79 and $165 \text{ gC gChla}^{-1}$ near the ocean surface.

Acknowledgments

We thank three anonymous reviewers for their very constructive comments. Data management for PIRATA moorings is conducted by the TAO project office at NOAA/PMEL in collaboration with many research institutes listed on the PIRATA website (<http://www.pmel.noaa.gov/pirata>). We thank the chief scientist of the EGEE/AMMA project, Bernard Bourlès of Institut de Recherche pour le Développement (IRD) Brest and Nathalie Lefèvre (IRD LOCEAN) responsible for $f\text{CO}_2$ CARIOCA measurements on PIRATA moorings and provide us these data. DIC and TA of EGEE cruises have been analyzed by the SNAPO-CO2 national service of Institut National des Sciences de l'Univers (INSU) dedicated to the analysis of CO_2 ocean parameters. We thank the EGEE program for the measurement of nitrate. We thank Nathalie Lefèvre for her advice on the use of the biogeochemical model. We are indebted to Liliane Merlivat, Sabine Arnault, and Nicolas Kolodziejczyk for very fruitful discussions about biological production and ocean circulation. We are grateful to Nicolas Martin for sharing his programs to process the CARIOCA data. We thank Christopher Brown and David Sproson for the proofreading. The research leading to these results was supported through EU FP7 project CARBOCHANGE changes in carbon uptake and emissions by oceans in a changing climate which received funding from the European Commissions Seventh Framework Programme under grant agreement 264879.

References

- Alford, M. H. (2003), Redistribution of energy available for ocean mixing by long-range propagation of internal waves, *Nature*, 423(6936), 159–162, doi:10.1038/nature01628.
- Alford, M. H., and R. Pinkel (2000), Observations of overturning in the thermocline: The context of ocean mixing, *J. Phys. Oceanogr.*, 30, 805–832, doi:10.1175/1520-0485(2000)0300805.
- Bahamón, N., Z. Velásquez, and A. Cruzado (2003), Chlorophyll a and nitrogen flux in the Tropical North Atlantic ocean, *Deep Sea Res., Part I*, 50(10), 1189–1203, doi:10.1016/S0967-0637(03)00145-6.
- Bougeault, P., and P. Lacarrere (1989), Parameterization of orography-induced turbulence in a mesobeta-scale model, *Mon. Weather Rev.*, 117(8), 1872–1890, doi:10.1175/1520-0493.
- Bourlès, B., et al. (2007), African monsoon multidisciplinary analysis (AMMA): Special measurements in the Tropical Atlantic, *CLIVAR Exch.*, 12(2), 7–9.
- Bourlès, B., et al. (2008), The PIRATA program: History, accomplishments, and future directions, *Bull. Am. Meteorol. Soc.*, 89, 1111–1125.
- Boutin, J., and L. Merlivat (2009), New in situ estimates of carbon biological production rates in the Southern ocean from CARIOCA drifter measurements, *Geophys. Res. Lett.*, 109, L13608, doi:10.1029/2009GL038307.
- Da Silva, J. C. B., A. L. New, M. A. Srokosz, and T. J. Smyth (2002), On the observability of internal tidal waves in remotely-sensed ocean colour data, *Geophys. Res. Lett.*, 29(12), 1569–1573, doi:10.1029/2001GL013888.
- de Boyer Montégut, C., G. Madec, A. S. Fischer, A. Lazar, and D. Ludicone (2004), Mixed layer depth over the global ocean: An examination of profile data and a profile-based climatology, *J. Geophys. Res.*, 109, C12003, doi:10.1029/2004JC002378.
- Dickson, A., and F. Millero (1987), A comparison of the equilibrium constants for the dissociation of carbonic acid in seawater media, *Deep Sea Res., Part A*, 34(10), 1733–1743.
- Dourado, M., and G. Caniaux (2004), One-dimensional modeling of the oceanic boundary layer using PIRATA data at 10°S , 10°W , *Rev. Bras. Meteorol.*, 19(2), 217–226.
- Egbert, G. D., and R. D. Ray (2003), Semi-diurnal and diurnal tidal dissipation from TOPEX/Poseidon altimetry, *Geophys. Res. Lett.*, 30(17), 1907, doi:10.1029/2003GL017676.
- Garcia, H. E., R. A. Locarnini, T. P. Boyer, J. I. Antonov, O. K. Baranova, M. M. Zweng, J. R. Reagan, and D. R. Johnson (2014), Dissolved inorganic nutrients (phosphate, nitrate, silicate), in *World Ocean Atlas 2013, NOAA Atlas NESDIS 76*, vol. 4, edited by S. Levitus and A. Mishonov, pp. 1–25, Maryland National Oceanography Data Centre, Silver Spring, Md.
- Garrett, C., and W. Munk (1975), Space-time scales of internal waves: A progress report, *J. Geophys. Res.*, 80(3), 291–297, doi:10.1029/JC080i003p00291.
- Gaspar, P., Y. Grégoris, and J. M. Lefevre (1990), A simple eddy kinetic energy model for simulations of the oceanic vertical mixing: Tests at station Papa and long-term upper ocean study site, *J. Geophys. Res.*, 95(C9), 16,179–16,193, doi:10.1029/JC095iC09p16179.
- Geider, R., H. MacIntyre, and T. Kana (1997), Dynamic model of phytoplankton growth and acclimation: Responses of the balanced growth rate and the chlorophyll a:carbon ratio to light, nutrient-limitation and temperature, *Mar. Ecol. Prog. Ser.*, 148, 187–200.
- Geider, R., H. MacIntyre, and T. Kana (1998), A dynamic regulatory model of phytoplanktonic acclimation to light, nutrients, and temperature, *Limnol. Oceanogr.*, 43(4), 679–694.
- Gregg, M. C. (1989), Scaling turbulent dissipation in the thermocline, *J. Geophys. Res.*, 94(C7), 9686–9698, doi:10.1029/JC094iC07p09686.
- Gruber, N., C. D. Keeling, and N. R. Bates (2002), Interannual variability in the North Atlantic ocean carbon sink, *Science*, 298(5602), 2374–2378, doi:10.1126/science.1077077.
- Herbland, A. (1983), Chlorophyll maximum in the Eastern Tropical Atlantic Ocean: Description, ecology interpretation, *Oceanogr. Trop.*, 18(2), 295–318.
- Jardon, F. P., P. Bouruet-Aubertot, Y. Cuyppers, F. Vivier, and A. Lourenco (2011), Internal waves and vertical mixing in the Storfjorden Polynya, Svalbard, *J. Geophys. Res.*, 116, C12040, doi:10.1029/2010JC006918.
- Josse, J. (1992), Modélisation couplée océan-atmosphère à méso-échelle: Application à la campagne SEMAPHORE, PhD thesis, Univ. Toulouse, Toulouse, France.

- Kahru, M. (1983), Phytoplankton patchiness generated by long internal waves: A model, *Mar. Ecol. Prog. Ser.*, *10*(2), 111–117, doi:10.3354/meps010111.
- Kantha, L. H., and C. A. Clayson (1994), An improved mixed layer model for geophysical applications, *J. Geophys. Res.*, *99*(C12), 25,235–25,266, doi:10.1029/94JC02257.
- Key, R. M., A. Kozyr, C. L. Sabine, K. Lee, R. Wanninkhof, J. L. Bullister, R. A. Feely, F. J. Millero, C. Mordy, and T. H. Peng (2004), A global ocean carbon climatology: Results from global data analysis project (GLODAP), *Global Biogeochem. Cycles*, *18*, GB4031, doi:10.1029/2004GB002247.
- Koffi, U., N. Lefèvre, G. Kouadio, and J. Boutin (2010), Surface CO₂ parameters and air-sea CO₂ flux distribution in the Eastern Equatorial Atlantic, *J. Mar. Syst.*, *82*(3), 135–144, doi:10.1016/j.jmarsys.2010.04.010.
- Kolmogorov, A. N. (1942), Equations of turbulent motion of an incompressible fluid, *Izv. Akad. Nauk SSSR, Ser. Fiz.*, *6*(1/2), 56–58.
- Kolodziejczyk, N., B. Bourlès, F. Marin, J. Grelet, and R. Chuchla (2009), Seasonal variability of the Equatorial Undercurrent at 10°W as inferred from recent in situ observations, *J. Geophys. Res.*, *114*, C6014, doi:10.1029/2008JC004976.
- Large, W., J. McWilliams, and S. Doney (1994), Oceanic vertical mixing—A review and a model with a non local boundary-layer parametrization, *Rev. Geophys.*, *32*(4), 363–403, doi:10.1029/94RG01872.
- Lefèvre, N., and L. Merlivat (2012), Carbon and oxygen net community production in the Eastern Tropical Atlantic estimated from a moored buoy, *Global Biogeochem. Cycles*, *26*, GB1009, doi:10.1029/2010GB004018.
- Lefèvre, N., and A. Taylor (2002), Estimating pCO₂ from sea surface temperatures in the Atlantic gyres, *Deep Sea Res., Part I*, *49*(3), 539–554.
- Lefèvre, N., A. Taylor, F. J. Gilbert, and R. Geider (2003), Modeling carbon to nitrogen and carbon to chlorophyll a ratios in the ocean at low latitudes: Evaluation of the role of physiological plasticity, *Limnol. Oceanogr. Methods*, *48*(5), 1796–1807.
- Lefèvre, N., A. Guillot, L. Beaumont, and T. Danguy (2008), Variability of fCO₂ in the Eastern Tropical Atlantic from a moored buoy, *J. Geophys. Res.*, *113*, C01015, doi:10.1029/2007JC004146.
- Leinweber, A., N. Gruber, H. Fenzel, G. E. Friedeich, and F. P. Chavez (2009), Diurnal carbon cycling in the surface ocean and lower atmosphere of Santa Monica Bay, California, *Geophys. Res. Lett.*, *36*, L08601, doi:10.1029/2008GL037018.
- Lévy, M., R. Ferrari, P. J. S. Franks, A. P. Martin, and P. Rivière (2012), Bringing physics to life at the submesoscale, *Geophys. Res. Lett.*, *39*, L14602, doi:10.1029/2012GL052756.
- Liccardo, A., A. Fierro, D. Ludicone, P. Bouruet-Aubertot, and L. Dubroca (2013), Response of the deep chlorophyll maximum to fluctuations in vertical mixing intensity, *Prog. Oceanogr.*, *109*, 33–46, doi:10.1016/j.pocean.2012.09.004.
- Merbach, C., C. H. Culberson, and J. E. Hawley (1973), Measurements of the apparent dissociation constants of carbonic acid in seawater of atmospheric pressure, *Limnol. Oceanogr.*, *18*(6), 897–907.
- Muacho, S., J. C. B. da Silva, V. Brotas, and P. B. Oliveira (2013), Effect of Internal Waves on near-surface chlorophyll concentration and primary production in the nazaré Canyon (West of the Iberian Peninsula), *Deep Sea Res., Part I*, *89*, 89–96, doi:10.1016/j.dsr.2013.07.012.
- Nycander, J. (2005), Generation of internal waves in the deep ocean by tides, *J. Geophys. Res.*, *110*, C10028, doi:10.1029/2004JC002487.
- Osborn, T. R. (1980), Estimates of the local rate of vertical diffusion from dissipation measurements (ocean turbulence), *J. Phys. Oceanogr.*, *10*, 83–89, doi:10.1175/1520-0485(1980)010<0083:EOTLRO>2.0.CO;2.
- Oschlies, A. (2002), Nutrient supply to the surface waters of the North Atlantic: A model study, *J. Geophys. Res.*, *107*(C5), 3046, doi:10.1029/2000JC000275.
- Oschlies, A., and V. Garçon (1998), Eddy-induced enhancement of primary production in a model of the North Atlantic ocean, *Nature*, *394*(6690), 266–269.
- Parard, G. (2011), Etude de la variabilité de la fugacité du CO₂ dans l'Atlantique Tropical: de l'échelle diurne à saisonnière, PhD thesis, Univ. Pierre et Marie Curie, Paris VI.
- Parard, G., N. Lefèvre, and J. Boutin (2010), Sea water fugacity of CO₂ at the PIRATA mooring at 6°S, 10°W, *Tellus, Ser. B*, *62B*(5), 636–648, doi:10.1111/j.1600-0889.2010.00503.x.
- Park, Y.-H. H., J.-L. L. Fuda, I. Durand, and A. C. Naveira Garabato (2008), Internal tides and vertical mixing over the Kerguelen Plateau, *Deep Sea Res., Part II*, *55*(5), 582–593, doi:10.1016/j.dsr2.2007.12.027.
- Paulson, C., and J. Simpson (1977), Irradiance measurements in the upper ocean, *J. Phys. Oceanogr.*, *7*, 952–956.
- Planas, D., S. Agustí, C. M. Duarte, T. C. Granata, and M. Merino (1999), Nitrate uptake and diffusive nitrate supply in the Central Atlantic, *Limnol. Oceanogr.*, *44*(1), 116–126.
- Redelsperger, J. L., A. Diedhiou, C. Flamant, S. Janicot, J. P. Lafore, T. Lebel, J. Polcher, G. Caniaux, P. Rosnay, and M. Desbois (2006), AMMA, une étude multidisciplinaire de la mousson ouest-africaine, *La Météorologie*, *54*, 22–32.
- Robinson, C., P. Serret, G. Tilstone, E. Teira, M. V. Zubkov, A. P. Rees, and E. M. S. Woodward (2002), Plankton respiration in the Eastern Atlantic ocean, edited by P. Blondel, *Deep Sea Res., Part I*, *49*(5), 787–813, doi:10.1016/S0967-0637(01)00083-8.
- Robinson, I. S. and J. Da Silva (2010), Internal wave, in *Understanding the Oceans From Space: The Unique Applications of Satellite Oceanography*, vol. 12, pp. 453–483, Springer, Berlin.
- Schafstall, J., M. Dengler, P. Brandt, and H. Bange (2010), Tidal-induced mixing and diapycnal nutrient fluxes in the Mauritanian upwelling region, *J. Geophys. Res.*, *115*, C10014, doi:10.1029/2009JC005940.
- Sharples, J., C. M. Moore, and E. R. Abraham (2001), Internal tide dissipation, mixing, and vertical nitrate flux at the shelf edge of NE New Zealand, *J. Geophys. Res.*, *106*(C7), 14,069–14,081, doi:10.1029/2000JC000604.
- Sharples, J., J. F. Tweddle, J. A. M. Green, M. R. Palmer, Y. N. Kim, E. Hickman, P. M. Holligan, T. P. Rippeth, J. H. Simpson, and V. Kriktsov (2007), Spring-neap modulation of internal tide mixing and vertical nitrate fluxes at a shelf edge in summer, *Limnol. Oceanogr. Methods*, *52*(5), 1735–1747.
- Shih, L. H., J. R. Koseff, G. N. Ivey, and J. H. Ferziger (2005), Parameterization of turbulent fluxes and scales using homogeneous sheared stably stratified turbulence simulations, *J. Fluid Mech.*, *525*, 193–214, doi:10.1017/S0022112004002587.
- St. Laurent, L., and C. Garrett (2002), The role of internal tides in mixing the deep ocean, *J. Phys. Oceanogr.*, *32*(10), 2882–2899.
- Sweeney, C., E. Gloor, A. R. Jacobson, R. M. Key, M. McKinley, J. L. Sarmiento, and R. Wanninkhof (2007), Constraining global air-sea gas exchange for CO₂ with recent bomb 14C measurements, *Global Biogeochem. Cycles*, *21*, GB2015, doi:10.1029/2006GB002784.
- Takahashi, T., J. Olafsson, J. G. Goddard, D. W. Chipman, and S. C. Sutherland (1993), Seasonal variation of CO₂ and nutrients in the high-latitude surface oceans: A comparative study, *Global Biogeochem. Cycles*, *7*(4), 843–878, doi:10.1029/93GB02263.
- Taylor, A. H., A. J. Watson, M. Ainsworth, J. E. Robertson, and D. R. Turner (1991), A modelling investigation of the role of phytoplankton in the balance of carbon at the surface of the North Atlantic, *Global Biogeochem. Cycles*, *5*(2), 151–171, doi:10.1029/91GB00305.
- Taylor, K. E. (2001), Summarizing multiple aspects of model performance in a single diagram, *J. Geophys. Res.*, *106*(D7), 7183–7192, doi:10.1029/2000JD900719.
- Thomas, H., S. E. Craig, B. J. W. Greenan, W. Burt, G. J. Herndl, S. Higgingson, L. Salt, E. H. Shadwick, and J. Urrego-Blanco (2012), Direct observations of diel biological CO₂ fixation on the scotian shelf, Northwestern Atlantic ocean, *Biogeosciences*, *9*(6), 2301–2309, doi:10.5194/bg-9-2301-2012.

- Tyrell, T., and A. H. Taylor (1995), Latitudinal and seasonal variations in carbon dioxide and oxygen in the Northeast Atlantic and the effects on *Emiliana huxleyi* and other phytoplankton, *Global Biogeochem. Cycles*, *9*(4), 585–604, doi:10.1029/95GB01133.
- Veldhuis, M. J. W., K. R. Timmermans, P. Croot, and B. Van Der Wagt (2005), Picophytoplankton: A comparative study of their biochemical composition and photosynthetic properties, *J. Sea Res.*, *53*(1–2), 7–24, doi:10.1016/j.seares.2004.01.006.
- Voituriez, B., and A. Herbland (1977), Etude de la production pélagique de la zone équatoriale de l'Atlantique à 4°W. Relations entre la structure hydrologique et la production primaire, *Ser. Oceanogr.*, *15*(4), 313–331.
- Wade, M., G. Caniaux, Y. du Penhoat, M. Dengler, H. Giordani, and R. Hummels (2010), A one-dimensional modeling study of the diurnal cycle in the Equatorial Atlantic at the PIRATA buoys during the EGEE-3 campaign, *Ocean Dyn.*, *61*, 1–20, doi:10.1007/s10236-010-0337-8.
- Wang, X. J., M. Behrenfeld, R. L. Borgne, R. Murtugudde, and E. Boss (2009), Regulation of phytoplankton carbon to chlorophyll ratio by light, nutrients and temperature in the Equatorial Pacific Ocean: A basin-scale model, *Biogeosciences*, *6*(3), 391–404.
- Wanninkhof, R., et al. (2013), Global ocean carbon uptake: Magnitude, variability and trends, *Biogeosciences*, *9*(8), 10,961–11,012, doi:10.1007/s10236-010-0337-8.
- Weill, A., et al. (2003), Toward a better determination of turbulent air-sea fluxes from several experiments, *J. Clim.*, *16*(4), 600–618.
- Xie, X. H., Y. Cuypers, P. Bouruet Aubertot, P. B. Ferron, A. Pichon, A. Lonrenço, and N. Cortes (2013), Large-amplitude internal tides, solitary waves, and turbulence in the central Bay of Biscay, *Geophys. Res. Lett.*, *40*, 2748–2754, doi:10.1002/grl.50533.